Infrared Near-Field Transducer for Heat-Assisted Magnetic Recording

Anurup Datta and Xianfan Xu

School of Mechanical Engineering and Birck Nanotechnology Center, Purdue University, West Lafayette, IN 47907 USA

Heat-assisted magnetic recording (HAMR) is one of the next generation data storage technologies that aims to increase the areal data density to beyond 1 TB/in^2. Near-field transducer (NFT), which is a type of plasmonic nanoscale antenna, is a key component of the HAMR system. The laser in an HAMR system typically operates in the near infrared wavelength range between 700–900 nm. We explore the plasmonic behavior and performance of a number of NFTs at longer wavelength of 1550 nm. The different plasmonic modes in the NFTs at different wavelengths are analyzed, and the correlation of the NFT performance with variations in the geometrical design is investigated. Thermal performances of NFT are also studied and compared with the thermal performances when NFTs are operated near 800 nm. It is found that there is a significant improvement in the figures of merit when using longer wavelengths and this can provide an important strategy to realize higher performance data storage devices.

Index Terms— **Heat-assisted magnetic recording (HAMR), near-field transducer (NFT).**

I. Introduction

FACING the increasing growth in the generation of digital data, there is a continuous demand for increased data storage capacity. Heat-assisted magnetic recording (HAMR) is one of the recent technologies which is poised to play a crucial role in achieving areal data density values of more than 1 TB/in^2 [1]–[4]. In an HAMR system, a highly anisotropic magnetic material is used as the recording medium which has a high value of coercivity to prevent random thermal destabilization of the very small sized individual bits at room temperature [5]. At the core of the HAMR system is a plasmonic metal antenna, also called near-field transducer (NFT) which helps to focus the energy from a diode laser into a very small volume much beyond the diffraction limit of light, into the recording medium and subsequently, heating up the medium locally. Increasing the recording medium temperature close to the Curie temperature decreases the coercivity of the medium and the magnetic switching field of the medium reduces. Thus, it is possible to orient the bits in the required orientation with the external magnetic field during the write cycle.

The key factor governing the performance of an HAMR system is the efficiency of the plasmonic nano antenna in delivering the requisite energy into a small volume to heat up the recording medium and simultaneously ensuring that the rise in the temperature of the NFT is kept to a minimum. Gold is the preferred choice of the material of the NFT due to its chemical stability, a good plasmonic behavior and high thermal conductivity [6]. However, the excessive rise in the temperature of the NFT is severely detrimental since it causes thermal reliability issues, possible deformation of the gold layer, thermal expansion of the NFT, and depletion of lubricant layer [7]–[10]. Thus, it is necessary to find a way to reduce the temperature rise of NFT without reducing the power delivery to the recording medium. In order to address this issue, several strategies have been proposed such as a two stage heating of the recording medium, where the recording medium is heated to an intermediate temperature by a laser waveguide and in the second stage the NFT heats up the medium to raise its temperature beyond the Curie point [11]. It was also shown that the introduction of a tapered geometry in the NFT design helps to increase the coupling efficiency as well decrease the temperature rise of the NFT [12]. Instead of using a continuous wave laser, pulsed laser heating can also serve to lower the temperature rise of the NFT [13].

In most of the studies related to HAMR, a semiconductor diode laser working in the wavelength range of 700–900 nm has been used as the source of heat, primarily due to the availability of lasers in this wavelength range. The possibility of using a laser in the longer near-IR wavelength range (1–2 μm) as the working wavelength of the NFT remains to be explored. Since the absorptivity of gold reduces rapidly with the increase in wavelength, operating in the higher wavelength regime can provide an alternate way to reduce the temperature rise of the NFT. According to Rayleigh scattering theory (if the critical dimension of a specific design of NFT is much less than the wavelength of light), the scattering decreases with the increase in wavelength; while according to Mie scattering theory (if the critical dimension of an NFT is comparable to the wavelength), the scattering from the NFT does not change with the increase in the wavelength, hence working in the higher wavelength regime should not cause additional issues to the surrounding components of an NFT in an HAMR system due to scattering.

In this paper, we study the wavelength-dependent characteristics of the coupling efficiency of the incident laser energy to the recording medium and the associated temperature rise of NFT. A triangle shaped NFT, which has one of the simplest geometry, was studied and the different plasmonic modes of NFT at different wavelengths are discussed. Also the shift in the resonance of the different plasmonic modes with the

Manuscript received January 5, 2017; revised May 26, 2017 and July 2, 2017; accepted August 9, 2017. Date of publication August 23, 2017; date of current version November 16, 2017. Corresponding author: X. Xu (e-mail: xxu@ecn.purdue.edu).

Color versions of one or more of the figures in this paper are available online at http://ieeexplore.ieee.org.

Digital Object Identifier 10.1109/TMAG.2017.2743078

TABLE I
MATERIALS AND PROPERTIES USED IN THE CALCULATION

Material	Optical Properties			Thermal Properties		
	Thickness [nm]	n	k	Vertical thermal conductivity (W/mK)	Lateral thermal conductivity (W/mK)	Density x Specific Heat (ρ^*c_p) (J/m^3-K) x10^6
Heat sink	100	0.26	5.28	150	150	3.3
Interlayer	15	1.7	0	10	10	1.9
Storage medium	10	-	-	7	1.5	3.2
Media overcoat	2.5	2.3	0	2	2	1.76
Air	2.5	1	0	0.02	0.02	0.001225
Lube	1	1	0	0.02	0.02	0.001225
Head overcoat	2.5	2.5	0	2	2	1.76
NFT - Au	t	-	-	314	314	2.5

The optical properties of the storage medium and the NFT are wavelength dependent, they are not mentioned in this table.

change in the NFT dimension is elaborated. For comparative performance of the NFTs across different dimensions and different wavelengths, the media stack composition and dimensions, incident beam profile and model configuration are all kept constant and the variation of the coupling efficiency and its resonance condition is studied. We particularly focus on the 1550 nm wavelength since laser diodes at this wavelength are already available for telecommunication. An NFT design which is resonant at 1550 nm is chosen and its thermal performance is compared with an NFT at 800 nm. The optical and thermal performance of an E antenna at the two wavelengths is also discussed. It is found that it is possible to have a significant improvement in the thermal figure of merit by operating the working wavelength of NFT at 1550 nm.

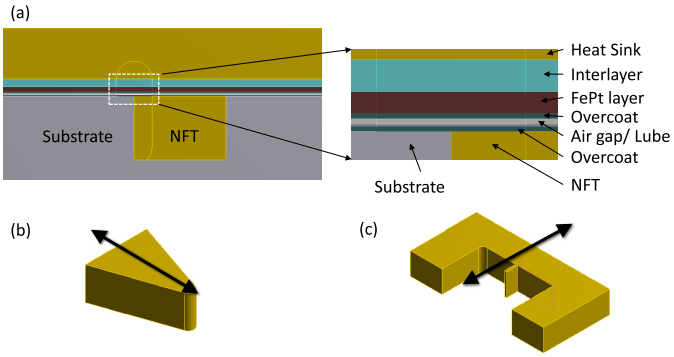

Fig. 1. (a) Schematic of the simulation model showing the different layers of the recording medium and the NFT. (b) Diagram of a triangle NFT. (c) Diagram of an E antenna NFT. The black arrows in (b) and (c) represent the incident polarization direction.

II. DESCRIPTION OF THE SIMULATION MODELS

A. Electromagnetic Simulation

Full-wave 3-D electromagnetic simulations were carried out using ANSYS HFSS which is a commercial finite element method based solver. In our simulations, the media stack was assumed to have several layers such as media overcoat, storage layer, interlayer, and the heat sink layer as described in Fig. 1(a). A 2.5 nm air gap separated the media stack from the NFT head. The NFT was considered to be embedded in a glass substrate with an over coat layer such as diamond-like carbon [14] for protection. Isometric models of the triangle NFT and the E antenna NFT are shown in Fig. 1(b) and (c), respectively. The NFT was made of gold and the storage medium was considered to be a FePt layer of 10 nm thick. Wavelength-dependent optical properties for gold were obtained from Johnson and Christy [15] and that for FePt was obtained from Cen *et al.* [16]. A Gaussian beam of diameter 600 nm was incident on the NFT and the polarization was set along the axis of the triangle for the triangle NFT and along the longitudinal axis of the notch for the E antenna NFT as shown by the black arrows in Fig. 1(b) and (c), respectively. Absorbing boundary conditions which radiate into the open space were considered at the outer surfaces of the model. While the thermal properties of the different layers in the medium stack might not precisely be known, representative values are used which are kept constant across all the models. This would allow to compare the relative thermal performance across the different models and wavelengths. Table I summarizes the optical and thermal properties of the different layers in the simulation model and their respective thicknesses.

For calculating the coupling efficiency of the system, the power absorbed in a cylindrical disk of diameter 70 nm in the recording medium layer was calculated and divided by the net incident power in the Gaussian beam. From the field solutions, the absorption profile within the NFT and the recording medium was calculated. We also consider the NFT absorption percentage which is the total power absorbed by the NFT divided by the incident power as a metric related to the temperature rise of the NFT.

B. Thermal Simulation

Using the results from the electromagnetic simulation, subsequent thermal simulations were performed using ANSYS Workbench. The geometry of the simulation model was exactly the same as that in the electromagnetic model. The absorption within the NFT and the recording medium was treated as a volumetric heat generation term in the context

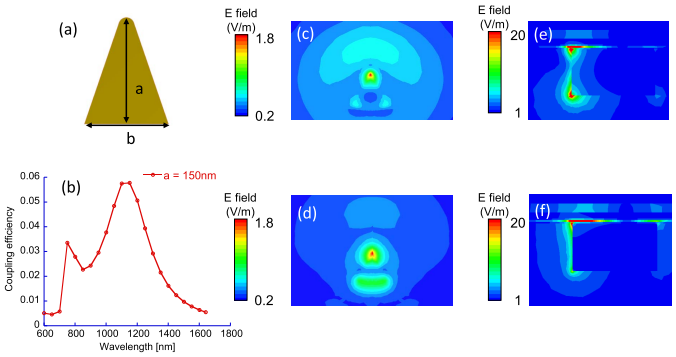

Fig. 2. (a) Geometry of the triangle NFT with the relevant dimensions. (b) Spectral plot of the coupling efficiency of the NFT with dimensions, $a = 150$ nm, $b = 150$ nm, and $t = 80$ nm. (c) Electric field plot at the surface of the recording medium at 750 nm. (d) Electric field plot at the surface of the recording medium at 1150 nm. (e) Cross-sectional electric field plot at 750 nm. (f) Cross-sectional electric field plot at 1150 nm.

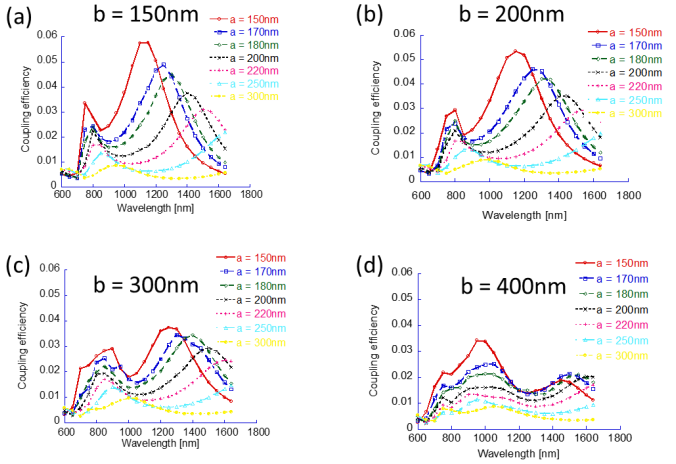

Fig. 3. Spectral plot of the coupling efficiency for various dimensions of the triangle antenna. (a) $b = 150$ nm and a is varied, (b) $b = 200$ nm and a is varied, (c) $b = 300$ nm and a is varied, and (d) $b = 400$ nm and a is varied.

of the thermal simulation [17]. For all the thermal simulations, it was assumed that the incident power was 10 mW. Steady-state simulation was performed for the NFT and a convection heat transfer coefficient of 1.7×10^5 W/mK was considered on the air bearing side [18], [19]. In contrast, the recording medium is typically heated for about one nanosecond and hence the temperature of the recording medium was calculated at the end of 1 ns.

The primary thermal figure of merit that was used for evaluating the performance of different designs was the ratio of the peak temperature rise in the medium at the end of 1 ns to the peak temperature rise of the NFT at steady state.

III. Results and Discussion

A. Plasmonic Modes of a Triangular NFT

We first study the spectral response of a triangular antenna with dimensions, as shown in Fig. 2(a): $a = 150$ nm, $b = 150$ nm, and $t = 80$ nm where t is the thickness of the NFT. The coupling efficiency into the recording medium is calculated as a function of the wavelength and is shown in Fig. 2(b). It is shown from Fig. 2(b) that there are two resonant peaks associated with the triangle NFT where the coupling efficiency reaches a maximum. The origin of the different peaks can be attributed to two different plasmonic modes which get excited in the triangle antenna at different wavelengths. Fig. 2(c) and (d) shows the electric field profile at the recording medium surface corresponding to the two different peaks at 750 and 1150 nm. The electric field profile corresponding to 750 nm has a region of field concentration near the tip of the antenna. This mode is similar to a Fabry–Perot type of resonance mode, where the electric field is maximum at the top and bottom of the antenna tip and reaches a minimum near the middle of the thickness [20]. This is observed from the cross-sectional electric field view in Fig. 2(e). On the other hand, the higher order plasmonic mode at 1150 nm has an additional charge concentration near the base of the triangle, as shown in Fig. 2(d), and the electric field as shown in Fig. 2(f) along the cross section does not vary significantly along the thickness of the antenna. In the subsequent discussion, we explore in detail about the relation of the resonance peak wavelengths with the dimensions of the triangle antenna.

Fig. 3(a) shows the coupling efficiency as a function of wavelength when the height a of the triangle is varied. It is found that with the increase in height, the position of the resonance peak moves toward the higher wavelength. The lower order resonance peak near 800 nm redshifts slowly while the position of the higher order resonance peak is more sensitive to the change in height. It is known that in a nanoparticle, when the polarization of the incident light is along its longer axis, with the increase in the length of the nanoparticle, the resonance peak shifts toward a longer wavelength [21]. We observe a similar effect in the triangular nano antenna. Fig. 3(b)–(d) shows the effect of change of resonance wavelength by changing the base of the triangle b. Fig. 3(b) shows the coupling efficiency as a function of wavelength when the height, a of the triangle is varied for a fixed $b = 200$ nm, Fig. 3(c) for a fixed $b = 300$ nm and Fig. 3(d) for fixed $b = 400$ nm. It is observed that the shift in the resonance peak for change in b is much less when compared to the resonance peak shift for change in a. At the same time higher values of b reduce the coupling efficiency. For example when b is increased to 400 nm in Fig. 3(d) for $a = 150$ nm, the first peak moves to around 1000 nm while the second peak moves to around 1450 nm and the magnitude of the second peak becomes much smaller. From these studies it is possible to choose a dimension of the triangular NFT which can work at a specified wavelength with maximized efficiency. For further comparison, we choose two designs, one resonant at 800 nm (dimensions: $a = 150$ nm, $b = 200$ nm, $t = 80$ nm, and tip radius of curvature $= 14$ nm) with a coupling efficiency of 2.7% and another resonant at 1550 nm (dimensions: $a = 220$ nm, $b = 150$ nm, $t = 80$ nm, and tip radius of curvature $= 14$ nm) with a coupling efficiency of 2.6% and assess their performances. It is found that with the increase in wavelength to 1550 nm, the optical spot size in the recording medium increases to 42 nm $\times$ 52 nm compared to 20 nm $\times$ 36 nm at a wavelength of 800 nm. The increase in spot size is primarily related to the increased wavelength. The absorption percentage for the NFT at 800 nm is 9.1%, compared to 2.6%

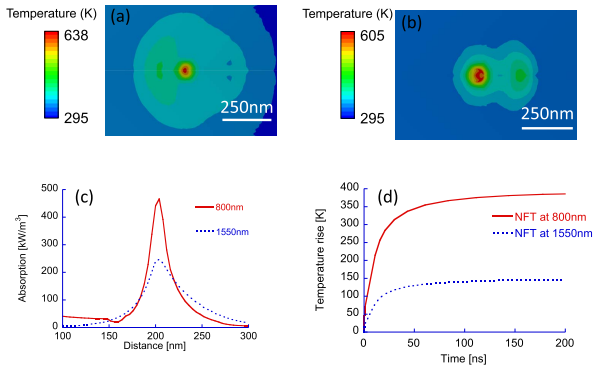

Fig. 4. Temperature plot of the recording medium at the end of 1 ns for (a) triangle NFT of dimensions $a = 150$ nm, $b = 200$ nm, $t = 80$ nm, and operating at 800 nm and (b) triangle NFT of dimensions $a = 220$ nm, $b = 150$ nm, $t = 80$ nm, and operating at 1550 nm. (c) Absorption profile in the recording medium at 800 and 1550 nm and (d) temporal temperature rise of the NFTs operating at 800 and 1550 nm, respectively.

for the NFT at 1550 nm, which shows a significant reduction in the power absorbed by the NFT at longer wavelengths that can benefit the thermal figures of merit.

B. Temperature Profile of the Triangular NFT and Recording Medium at Different Wavelengths

The temperature profile of the recording medium at the end of 1 ns is shown in Fig. 4(a) and (b). Fig. 4(a) shows the temperature profile of the recording medium when the working wavelength is 800 nm, and Fig. 4(b) shows the temperature profile for that at 1550 nm. It is seen that the temperature rise in the medium is almost similar due to the coupling efficiency being almost the same. The slightly higher temperature in the medium at 800 nm can be attributed to the fact that the peak temperature is dependent on the peak absorption in the medium, which is higher for 800 nm than 1550 nm, as shown in Fig. 4(c). The full width at half maxima (FWHM) thermal spot size at the recording medium is 63 nm × 78 nm at 800 nm while it is 97 nm × 108 nm at 1550 nm. The increase in thermal spot size is primarily related to the increased optical spot size at 1550 nm and tuning the geometrical parameters of the triangle NFT such as making the tip of NFT sharper cannot significantly reduce the spot size at longer wavelengths. Even if the tip radius of curvature is changed to 2 nm from 14 nm, the thermal spot size only reduces marginally to 90 nm × 98 nm at 1550 nm. Fig. 4(d) shows the temperature rise of the NFTs for 800 and 1550 nm up to the steady state. The NFTs reach a steady-state temperature within about 100 ns. However, it can be seen that the maximum steady-state temperature rise for the NFT at 800 nm is 390 K while the maximum temperature rise at 1550 nm is only 148 K. Thus, the thermal figure of merit (the ratio of the temperature rise in the media versus in NFT) at 800 nm is 0.88 while that at 1550 nm is 2.09, about a 2.38 times increase.

C. E antenna at Different Wavelengths

The E antenna NFT is one of the familiar NFT design in the HAMR community [22]. We also explore the performance of an E antenna at two different wavelengths and compare their optical and thermal performance. Fig. 5(a) shows the

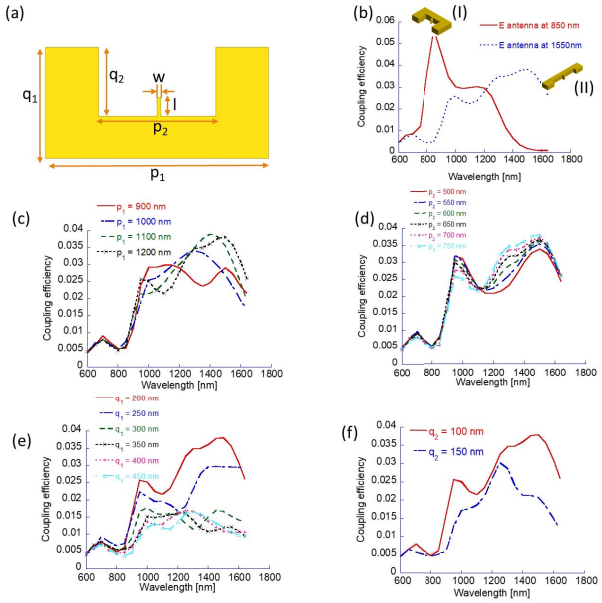

Fig. 5. (a) Schematic of an E antenna with the relevant dimensions. (b) Spectral dependence of the coupling efficiency of the E antenna for two different designs, one resonant at 850 nm and another resonant at 1550 nm. (c) Spectral dependence of the coupling efficiency of the E antenna when p_1 is varied. (d) Spectral dependence of the coupling efficiency of the E antenna when p_2 is varied. (e) Spectral dependence of the coupling efficiency of the E antenna when q_1 is varied. (f) Spectral dependence of the coupling efficiency of the E antenna when q_2 is varied.

schematic of the E antenna with the relevant dimensions, and Fig. 5(b) shows the wavelength dependence of the coupling efficiency for two different E antenna designs, one resonant at 850 nm and another at 1550 nm. The E antenna, resonant at 850 nm, which is denoted in Fig. 5(b) as design (I), has the dimensions of $w = 20$ nm, $l = 50$ nm, $t = 100$ nm, $p_1 = 600$ nm, $p_2 = 316$ nm, $q_1 = 300$ nm, and $q_2 = 186$ nm while the E antenna resonant at 1550 nm and denoted as design (II), has the dimensions of $w = 20$ nm, $l = 80$ nm, $t = 125$ nm, $p_1 = 1200$ nm, $p_2 = 750$ nm, $q_1 = 200$ nm, and $q_2 = 100$ nm. It is found that the maximum coupling efficiency at 850 nm is 5.8% while it is 3.8% at 1550 nm. From Fig. 5(b), we see that for each E antenna design, there are two peaks corresponding to a Fabry–Perot mode of resonance and a higher order mode of resonance. The resonance mode at 850 nm for the design (I) corresponds to the Fabry–Perot mode and the higher order mode is at 1200 nm. On the other hand, the resonance mode at 1550 nm for the design (II) corresponds to the higher order mode and a small peak corresponding to the Fabry–perot mode is seen at 900 nm. In order to optimize the NFT design at a particular wavelength, the relevant geometric parameters (w, l, t, p_1, p_2, q_1, and q_2) were varied to maximize the coupling efficiency at that wavelength. The dimensions p_1, p_2, q_1, and q_2 control the size of the rectangular window of the E antenna and are primarily responsible for resonantly transmitted power from the input to the exit plane of the E antenna while the notch dimensions (w and l) are responsible for the intense field concentration at the tip. Fig. 5(c)–(f) shows the change in the coupling efficiency as a function of wavelength as the dimensions p_1, p_2, q_1, and q_2 are varied systematically one by one

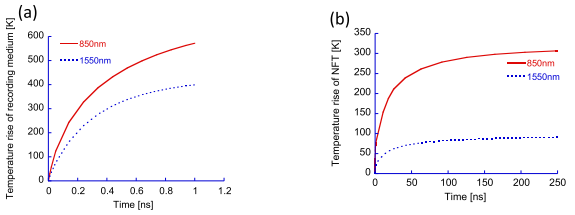

Fig. 6. (a) Temperature rise of the recording medium at the end of 1 ns for the two different E antenna NFTs, designs I and II, respectively. (b) Steady-state temperature rise of the NFTs for the two different designs.

keeping the other dimensions constant according to design (II). By suitable adjustments of these dimensions, the higher order resonance peak as seen in the curves in Fig. 5(c)–(f) can be modified. Fig. 5(c) and (d) shows the variation of the coupling efficiency when p_1 and p_2 are changed, respectively. It is seen that while changing the outer dimension, p_1 of the E antenna the resonance peak can be changed significantly, but the inner dimension, p_2 does not have any significant effect on the resonance peak position. On the other hand, having a lower value of q_1 gives a higher coupling efficiency at 1550 nm, as seen from Fig. 5(e). Also, by changing the dimension q_2, as shown in Fig. 5(f), the resonance characteristics of the E antenna can be modified. This optimization procedure helps in selecting an E antenna design resonant at a given wavelength.

Fig. 6(a) shows the recording medium temperature after 1 ns for the two designs of the NFT, and Fig. 6(b) shows the steady-state temperature of the NFT at 850 and 1550 nm. For the same incident power, the temperature rise in the medium is 1.4 times more at 850 nm than at 1550 nm due to the higher coupling efficiency and the temperature difference in the recording medium is evident even at time scales much less than 1 ns. However, at the same time, the peak temperature rise for the NFT at 850 nm is 3.39 times higher than that at 1550 nm. The NFT absorption at 1550 nm is 4.6% compared to 19.2% for the NFT at 850 nm which causes a higher peak temperature rise of the NFT at 850 nm. The thermal figure of merit for the NFT at 1550 nm is 4.33 versus 1.83 for the NFT at 850 nm. The thermal spot size (FWHM) at 1550 nm is 75 nm $\times$ 88 nm while that at 850 nm is 77 nm $\times$ 74 nm. In an E antenna, the thermal spot size depends both on the working wavelength as well as the dimension of the notch. Since the width, w of the notch is the same for both the designs, the corresponding thermal spot size also does not vary significantly between the two wavelengths.

IV. Conclusion

In summary, we investigated the performance of an HAMR system at longer near-IR wavelength range for two NFT designs, the triangle NFT, and the E antenna NFT. The different plasmonic modes generated in the NFTs at different wavelengths are discussed and their dependence on the geometry of the NFT is explained. Thermal simulation results are also presented for both the recording medium and the NFTs. It is found that it is possible to improve the thermal performance of the HAMR by a factor of 2–3 times by using longer wavelengths in the near-IR wavelength. The thermal spot size in the medium when using a longer wavelength is larger by about 50% in a triangular NFT, but the increase in an E antenna NFT is only a few percent. At longer wavelength, specifically 1550 nm, laser diode sources are readily available. The existing fabrication processes for the peripheral elements in an HAMR system such as the waveguide, input and output coupler should be scalable to different designs necessary for different NFT working wavelengths. This paper provides an important alternative strategy for the HAMR technology.

Acknowledgment

This work was supported by ASTC—the Advanced Storage Technology Consortium.

References

[1] R. E. Rottmayer *et al.*, "Heat-assisted magnetic recording," *IEEE Trans. Magn.*, vol. 42, no. 10, pp. 2417–2421, Oct. 2006.
[2] M. H. Kryder *et al.*, "Heat assisted magnetic recording," *Proc. IEEE*, vol. 96, no. 11, pp. 1810–1835, Nov. 2008.
[3] L. Pan and D. B. Bogy, "Data storage: Heat-assisted magnetic recording," *Nature Photon.*, vol. 3, no. 4, pp. 189–190, 2009.
[4] N. Zhou *et al.*, "Plasmonic near-field transducer for heat-assisted magnetic recording," *Nanophotonics*, vol. 3, no. 3, pp. 141–155, 2014.
[5] D. Weller and A. Moser, "Thermal effect limits in ultrahigh-density magnetic recording," *IEEE Trans. Magn.*, vol. 35, no. 6, pp. 4423–4439, Nov. 1999.
[6] W. A. Challener, E. Gage, A. Itagi, and C. Peng, "Optical transducers for near field recording," *Jpn. J. Appl. Phys.*, vol. 45, no. 8B, p. 6632, 2006.
[7] B. Xu *et al.*, "Thermal issues and their effects on heat-assisted magnetic recording system (invited)," *J. Appl. Phys.*, vol. 111, no. 7, p. 07B701, 2012.
[8] L. Wu, "Modelling and simulation of the lubricant depletion process induced by laser heating in heat-assisted magnetic recording system," *Nanotechnology*, vol. 18, no. 21, p. 215702, 2007.
[9] P. Yu, W. Zhou, S. Yu, and Y. Zeng, "Laser-induced local heating and lubricant depletion in heat assisted magnetic recording systems," *Int. J. Heat Mass Transf.*, vol. 59, pp. 36–45, Apr. 2013.
[10] B. Liu and Y. F. Han, "Writing induced nanodeformation and its effects on head-disk clearance," *J. Appl. Phys.*, vol. 93, no. 10, pp. 8716–8718, 2003.
[11] S. Xiong, J. Kim, Y. Wang, X. Zhang, and D. Bogy, "A two-stage heating scheme for heat assisted magnetic recording," *J. Appl. Phys.*, vol. 115, no. 17, p. 17B702, 2014.
[12] A. Datta and X. Xu, "Improved near-field transducer design for heat-assisted magnetic recording," *IEEE Trans. Magn.*, vol. 52, no. 12, Dec. 2016, Art. no. 3101306.
[13] B. Xu *et al.*, "Performance benefits from pulsed laser heating in heat assisted magnetic recording," *J. Appl. Phys.*, vol. 115, no. 17, p. 17B701, 2014.
[14] B. Marchon, T. Pitchford, Y.-T. Hsia, and S. Gangopadhyay, "The head-disk interface roadmap to an areal density of Tbit/in^2," *Adv. Tribol.*, vol. 2013, Feb. 2013, Art. no. 521086.
[15] P. B. Johnson and R. W. Christy, "Optical constants of the noble metals," *Phys. Rev. B, Condens. Matter*, vol. 6, no. 12, p. 4370, 1972.
[16] Z. Cen *et al.*, "Optical property study of FePt-C nanocomposite thin film for heat-assisted magnetic recording," *Opt. Exp.*, vol. 21, no. 8, pp. 9906–9914, 2013.
[17] N. Zhou, L. M. Traverso, and X. Xu, "Power delivery and self-heating in nanoscale near field transducer for heat-assisted magnetic recording," *Nanotechnology*, vol. 26, no. 13, p. 134001, 2015.
[18] N. Zuckerman and J. Fang, "Two carrier heat transfer modeling for heat assisted magnetic recording," in *Proc. ASME Heat Transf. Summer Conf. Collocated, ASME 7th Int. Conf. Energy Sustain., ASME 11th Int. Conf. Fuel Cell Sci., Eng. Technol.*, 2013, p. V001T03A006.
[19] H. Li, M. Kurita, J. Xu, and S. Yoshida, "Iteration method for analysis of write-current-induced thermal protrusion," *Microsyst. Technol.*, vol. 16, nos. 1–2, pp. 161–167, 2010.
[20] L. Ding, J. Qin, S. Guo, T. Liu, E. Kinzel, and L. Wang, "Resonant effects in nanoscale bowtie apertures," *Sci. Rep.*, vol. 6, Jun. 2016, Art. no. 27254.
[21] N. Berkovitch, P. Ginzburg, and M. Orenstein, "Nano-plasmonic antennas in the near infrared regime," *J. Phys., Condens. Matter*, vol. 24, no. 7, p. 073202, 2012.
[22] B. C. Stipe *et al.*, "Magnetic recording at 1.5 Pb m^{-2} using an integrated plasmonic antenna," *Nature Photon.*, vol. 4, no. 7, pp. 484–488, 2010.